

THE PER-TAU SHELL:
A GIANT STAR-FORMING SPHERICAL SHELL REVEALED BY 3D DUST OBSERVATIONS

SHMUEL BIALY^{1*}, CATHERINE ZUCKER¹, ALYSSA GOODMAN^{1,2}, MICHAEL M. FOLEY¹, JOÃO ALVES^{2,3}, VADIM A. SEMENOV¹,
ROBERT BENJAMIN⁴, REIMAR LEIKE^{5,6}, TORSTEN ENßLIN^{5,6}

ABSTRACT

A major question in the field of star formation is how molecular clouds form out of the diffuse Interstellar Medium (ISM). Recent advances in 3D dust mapping are revolutionizing our view of the structure of the ISM. Using the highest-resolution 3D dust map to date, we explore the structure of a nearby star-forming region, which includes the well-known Perseus and Taurus molecular clouds. We reveal an extended near-spherical shell, 156 pc in diameter, hereafter the “Per-Tau Shell”, in which the Perseus and Taurus clouds are embedded. We also find a large ring structure at the location of Taurus, hereafter, the “Tau Ring”. We discuss a formation scenario for the Per-Tau Shell, in which previous stellar and supernova (SN) feedback events formed a large expanding shell, where the swept-up ISM has condensed to form both the shell and the Perseus and Taurus molecular clouds within it. We present auxiliary observations of HI, H α , ²⁶Al, and X-rays that further support this scenario, and estimate Per-Tau Shell’s age to be $\approx 6 - 22$ Myrs. The Per-Tau shell offers the first three-dimensional observational view of a phenomenon long-hypothesized theoretically, molecular cloud formation and star formation triggered by previous stellar and SN feedback.

Subject headings: Interstellar medium (847) – Molecular clouds (1072) – Solar neighborhood (1509) – Stellar feedback (1602) – Superbubbles (1656) – Astronomy data visualization (1968)

1. INTRODUCTION

The conversion of diffuse gas into a dense-cold phase is the first step and a potential bottleneck for star formation. The balance between heating and cooling processes in the ISM results in a multiphase gas, consisting of the cold/warm neutral media (CNM/WNM; Field et al. 1969; Wolfire et al. 2003; Seifried et al. 2010; Saury et al. 2014; Bialy & Sternberg 2019). The CNM, being colder and denser, is the phase susceptible to molecule formation, gravitational collapse and star formation. Numerical simulations have shown that the WNM-to-CNM conversion takes place in converging flows where WNM is shock compressed and then radiatively cools, forming CNM (Hennebelle & Péroult 1999; Koyama & Inutsuka 2000, 2002; Audit & Hennebelle 2005; Vázquez-Semadeni et al. 2006; Heitsch et al. 2006; Inoue & Inutsuka 2008, 2009; Hennebelle & Inutsuka 2019). These flows naturally occur in expanding superbubbles (SB) powered by SN and winds from massive stars, introducing a positive feedback-loop for star formation: [star formation] \rightarrow [expanding shell] \rightarrow [gas compression] \rightarrow [gravitational collapse] \rightarrow [star formation] (e.g., Hartmann et al. 2002; Hosokawa & Inutsuka 2006; Ntormousi et al. 2011; Palouš 2014).

The formation of dense gas and stars in expanding shells has been observed in CO and HI spectral *position-position-velocity* (PPV) cubes and in 2D dust extinction maps (e.g. Su

et al. 2009; Lee & Chen 2009; Dawson et al. 2011, 2015; Mackey et al. 2017, see reviews by Elmegreen 2011; Dawson 2013). However, a major limitation with 2D extinction maps and PPV cubes is that they do not include information on the distance along the line-of-sight (LOS), and the data are limited to the 2D “plane-of-the sky.” This results in blending of structures along the LOS and a limited access to the real 3D structure of gas in the ISM. This is especially a problem for structures that are only marginally denser than the surrounding ISM, such as old SN remnants, which may be major drivers of WNM-CNM conversion, molecule formation and star formation triggering (see Fig. 2 in Inutsuka et al. 2015).

Since the advent of *Gaia* (Brown et al. 2018), rapid progress has been made in the field of 3D dust mapping, which leverages stellar distance and extinction estimates made by modeling photometry and astrometry to chart the 3D distribution of dust (Lallement et al. 2019; Green et al. 2019; Chen et al. 2019; Leike & Enßlin 2019). The basic idea is intuitive: starlight extinction measures the dust column density whereas a parallax measurement constrains the star’s distance. Synthesizing column densities and distances towards a large number of stars provides information on the dust 3D density. Recently, Leike et al. (2020, hereafter L20) extended this framework, combining metric Gaussian variational inference with Gaussian Processes to construct a 3D dust map of the solar neighborhood’s ISM at 1 pc resolution.

In this paper, we use the L20 data to study the 3D density structure of the ISM in the Taurus-Perseus star-forming region (see Fig. 1). This region is amongst the most thoroughly observed and studied star-forming regions in the Solar Neighborhood. When large-scale mapping of molecular gas first became feasible, Ungerechts & Thaddeus (1987, hereafter UT87) mapped the Perseus-Taurus region in ¹²CO, and included a section in their paper entitled “Are the Taurus and IC 348 (a prominent part of Perseus) Clouds Connected?.” In velocity space, the CO data show a smooth connecting bridge between Taurus and Perseus, suggesting that a physically con-

*sbialy@cfa.harvard.edu

¹ Center for Astrophysics | Harvard & Smithsonian, 60 Garden st., Cambridge, MA, 02138

² Radcliffe Institute for Advanced Study, Harvard University, 10 Garden Street, Cambridge, MA 02138, USA

³ University of Vienna, Department of Astrophysics, Türkenschanzstrasse 17, 1180 Wien, Austria

⁴ Department of Physics, University of Wisconsin–Whitewater, 800 West Main Street, Whitewater, WI 53190

⁵ Max Planck Institute for Astrophysics, Karl-Schwarzschildstraße 1, 85748 Garching, Germany

⁶ Ludwig-Maximilians-Universität, Geschwister-Scholl-Platz 1, 80539 Munich, Germany

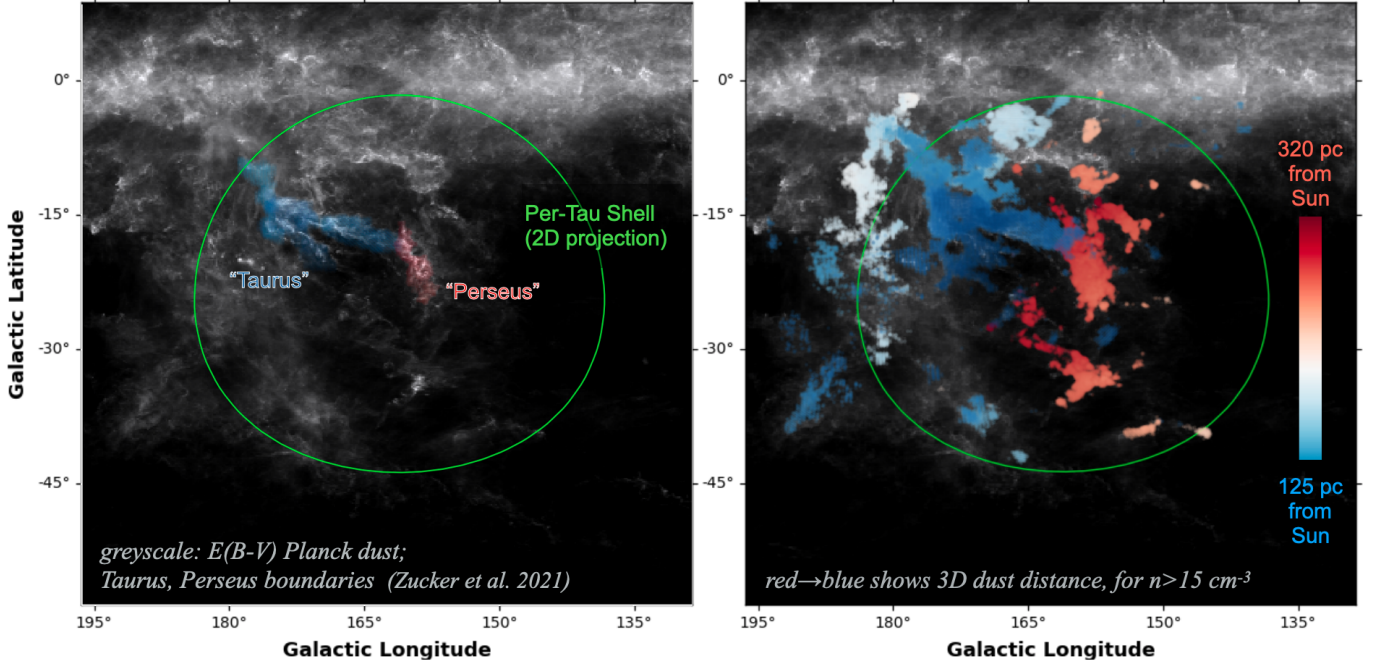


FIG. 1.— Finding Chart. **Left:** The Perseus-Taurus region as seen with Planck $E(B-V)$ dust (Abergel et al. 2014). The Taurus and Perseus molecular clouds are indicated (as defined in Zucker et al. 2021). **Right:** 2D Projection of 3D density structures (densities $n > 15 \text{ cm}^{-3}$) based on L20’s 3D dust map. While on the plane of the sky (as well as in velocity space; see Fig. 4a), the Perseus and Taurus clouds seem to connect, in practice they are separated by $\approx 150 \text{ pc}$ along the LOS. As we discuss in *this* paper, the two clouds are still related, as they both lie on two opposing ends of a large 3D shell, the “Per-Tau Shell.”

tinuous bridge of gas connecting the clouds is possible. But, as UT87 wisely suggested, velocity connection is not enough, and the plane-of-the-Sky “connection” of Taurus and Perseus could be a chance superposition.

We show that the connection between Taurus and Perseus is neither one of a physical bridge of gas or a “chance superposition.” Instead, Taurus and Perseus mark regions of compressed gas on opposite sides of an extended 3D SB, blown by SNe over the past $\sim 10 \text{ Myr}$.

2. OBSERVATIONAL DATA

We utilize the 3D dust extinction map recently published by L20. The data cover a region $(740 \text{ pc})^2$ wide in xy , and 570 pc tall in the z direction, where xyz are the Heliocentric Cartesian Galactic coordinates with the Sun at the origin. For each voxel in the data cube, L20 provide the opacity density per parsec: $s_x \equiv (\Delta\tau_G)/(\Delta L/\text{pc})$, where τ_G is the dust opacity in the *Gaia* G band, and $\Delta\tau_G/\Delta L$ is the difference in the *Gaia* G band dust opacity per unit length. The opacity density is proportional to the gas number density. Assuming a standard extinction curve, $A_G/N = 4 \times 10^{-22} \text{ mag cm}^2$ (Draine 2011), where A_G is *Gaia*’s G -band extinction and N is the hydrogen nuclei column density, we obtain

$$n = 880 s_x \text{ cm}^{-3}. \quad (1)$$

Here n is the number density of hydrogen nuclei, including both atomic and molecular phases. Applying this conversion factor to L20’s 3D dust data, we get n as a function of the 3D position, (x, y, z) throughout the cube. In this paper we focus on a subcube of the full map, spanning $x = [-340, -40] \text{ pc}$, $y = [-83, 217] \text{ pc}$, $z = [-238, 62] \text{ pc}$ and centered on the mid-distance of Perseus and Taurus.

In addition to the 3D data, we also make use of various 2D and PPV observations. We use Planck’s $E(B-V)$ dust (Abergel et al. 2014) and ^{12}CO from Dame et al. (2001) to

TABLE 1
SUMMARY OF NEW STRUCTURES IDENTIFIED

Name	Center Coordinates	Radius
Per-Tau Shell	$xyz = (-190, 65, -84) \text{ pc}$ $lbd = (161^\circ.1, -22^\circ.7, 218 \text{ pc})$ RA, Dec = $(53^\circ.0, 28^\circ.0)$	$R_s = 78 \text{ pc}$
Tau Ring	$xyz = (-174, 1, -44) \text{ pc}$ $lbd = (179^\circ.5, -14^\circ.2, 179 \text{ pc})$ RA, Dec = $(73^\circ.1, 21^\circ.3)$	$a = 39 \text{ pc}$ $b = 26 \text{ pc}$

xyz are the Heliocentric Cartesian Galactic coordinates, and lbd are Galactic longitude, latitude and distance from the sun. a and b are the semi-major and semi-minor axis (see also Appendix B).

explore the link between the 3D dust map and 2D observations. To trace past SN activity, we explore HI observations from HI4PI (Bekhti et al. 2016), $\text{H}\alpha$ observations from Finkbeiner (2003), ^{26}Al observations from COMPTEL (Diehl et al. 1995), and X-ray observations from ROSAT (Snowden et al. 1997) and from eROSITA’s public release image (see Appendix D).

All this observational data, as well as our 3D models (§3), are publicly available on Harvard’s DataVerse⁷.

3. RESULTS

In this section we explore the 3D structure of the Perseus-Taurus region, identifying the Per-Tau Shell, and the Tau Ring (§3.1-3.3, and Table 1). In §3.4 we compare these structures with 2D observations, and explore observational tracers of past SN activity which may have led to the formation of the Per-Tau Shell.

⁷ <https://doi.org/10.7910/DVN/6ODS8M>. Also included is the original *glue* session, which can be used to reproduce the figures as well as for further exploration.

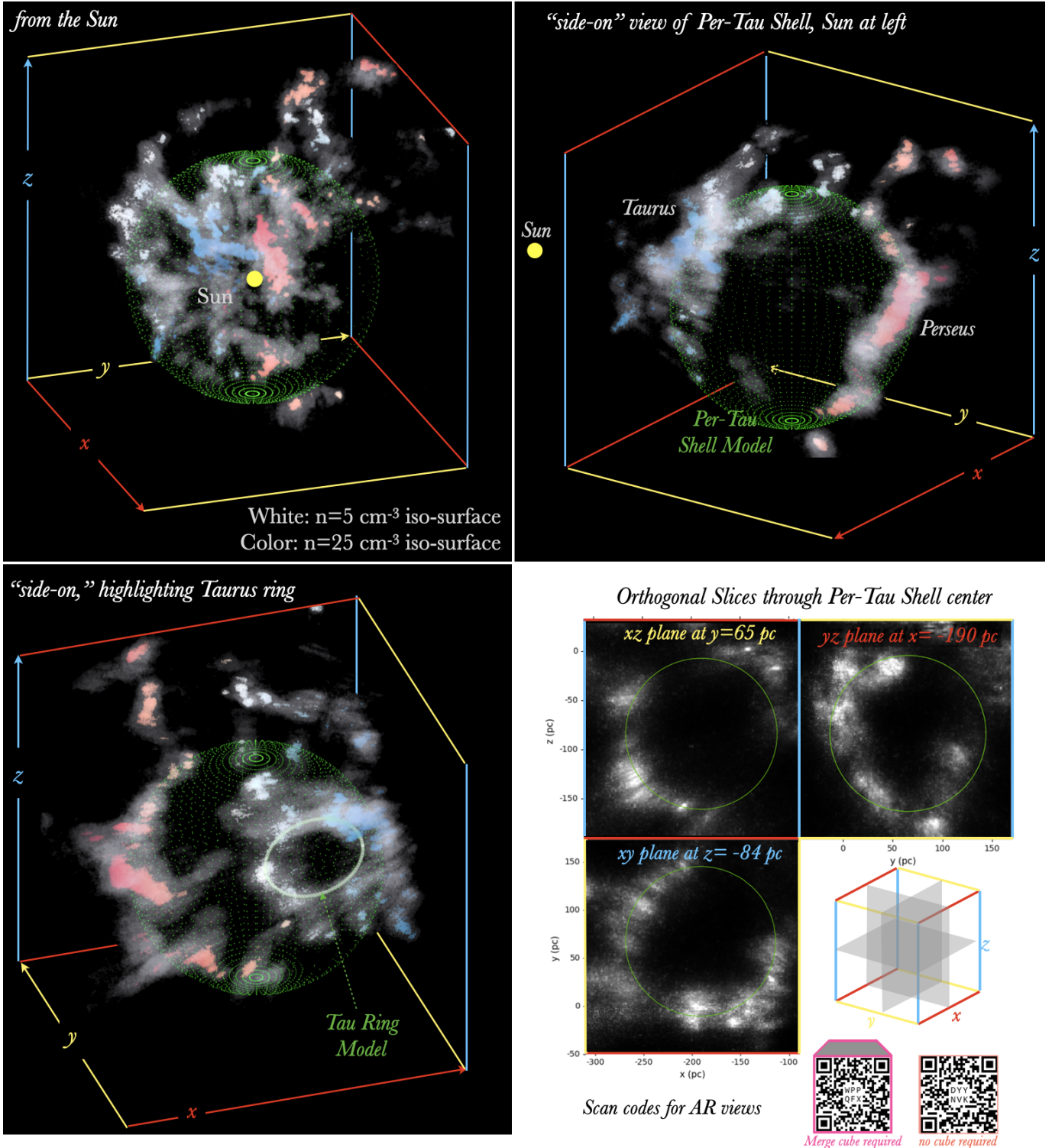


FIG. 2.— 3D views of the Per-Tau shell (for an interactive version of this figure click [here](https://faun.rc.fas.harvard.edu/czucker/Paper_Figures/sbially/pertau_superbubble.html)^a [b](#). See Fig. 5 for more static visualizations). Plotted are density iso-surfaces at levels $n = 5 \text{ cm}^{-3}$ (grey) and $n = 25 \text{ cm}^{-3}$ (color), overlaid with our spherical shell model, radius $R_s = 78 \text{ pc}$, distance from the sun $d = 218 \text{ pc}$. The $n = 25 \text{ cm}^{-3}$ surfaces are colored by distance from the sun (blue-to-red). **Upper-left:** View from the sun (compare with Fig. 1). **Upper-right:** A side view of the region. Perseus and Taurus and their diffuse envelopes are arranged on two opposing sides of the Per-Tau shell. **Lower-left:** Another side view emphasizing the Tau Ring. The ellipse is the Tau Ring model (Appendix B). **Lower-right:** 2D density slices along the xy , xz , yz planes. All planes intersect at shell’s center. In all panels xyz are the Heliocentric Cartesian Galactic Coordinates.

^a URL address for the interactive figure: https://faun.rc.fas.harvard.edu/czucker/Paper_Figures/sbially/pertau_superbubble.html.

^b For Augmented Reality (AR) experience, scan the QR codes with a mobile device (CoSpaces App required): Left code for viewing with a Merge Cube, right code for a tabletop AR. If you are already reading this article with a mobile device, click [here](#) (Merge Cube), or [here](#) (tabletop AR).

3.1. Per-Tau Shell

In Fig. 2 (see also the [interactive figure](#)^(a); for an augmented reality [AR] experience scan the QR code in Fig. 2 with a smartphone or a tablet) we present iso-surfaces of gas at $n = 5 \text{ cm}^{-3}$ (grey) and 25 cm^{-3} (color), for different viewing angles (see also Fig. 5). The color shows the distance from the sun. The density iso-surfaces reveal that the diffuse gas in the region is organized in a near-spherical geometry. The denser portion of the gas forms the Taurus and Perseus molecular clouds, lying on the near ($d \approx 150 \text{ pc}$) and far ($d \approx 300 \text{ pc}$) sides of the shell, respectively, where d is distance from the Sun.

We model the Per-Tau Shell as a spherical shell with radius $R_s = 78 \text{ pc}$, as shown in Fig. 2 and 5 (see Table 1 for the center coordinates). The model’s center was optimized by a visual inspection of the iso-surface data in 3D. The model’s radius was obtained by the position of the maximum in the radial density profiles, discussed in §3.3 below. In the bottom-right panel we show three density cuts through the shell’s center, along the planes xy , xz , yz . The density enhancements at $r = R_s$ are clearly evident.

We stress that the spherical-shell model only serves as an approximate representation of the real density structure. In practice, the shell geometry is more complex. The shell is not a perfect symmetric sphere, and it also exhibits significant density fluctuations (substructure). This is manifested as the “missing areas” in the shell’s iso-surfaces (Fig. 2, left), and the strong fluctuations in the density value in the density slices (Fig. 2, right). Such density fluctuations are expected to be present in the ISM due to supersonic turbulence and thermal instability (e.g., Federrath et al. 2008; Kritsuk et al. 2017; Bialy & Burkhardt 2020).

3.2. Tau Ring

Another interesting feature revealed by the 3D dust observations is a prominent ring structure at the location of the Taurus cloud (see Fig. 2), hereafter, the “Tau Ring”. The Tau Ring is well represented by an ellipse with semi-major axis $a = 39 \text{ pc}$ and semi-minor axis $b = 26 \text{ pc}$, centered on $\vec{r}_0 \approx (-174, 1, -44) \text{ pc}$, and viewed nearly edge-on along the LOS. In Appendix B we discuss Tau Ring’s orientation and detailed structure.

3.3. Radial Density Profiles of the Per-Tau Shell

In Fig. 3 we present the density profile of the Per-Tau shell, showing the radial mean density $\langle n \rangle_r$, density percentiles n_p , volume fractions f_V , and mass fractions f_M , as functions of the distance from the shell’s center, r . Each of these statistical quantities is computed within concentric spherical shells (Appendix A).

In Fig. 3 (top), $\langle n \rangle_r$ measures the mean radial trend in the region (averaging over many voxels at each radius). To illustrate the density dispersion within each radius, the solid colored curves show different density percentiles. The density percentiles span a significant range: for example, the 50-90 percentile spans 1 dex in density, and the 50-99.9 range is as large as 2 dex in density. The median density is below the mean, as expected for a lognormal density distribution. Overall, the mean and the density percentiles show a clear trend: increasing with r at small radii; peaking at $R_s = 78 \text{ pc}$, and then decreasing with r at larger radii.

In the middle and lower panels, we show the volume and mass fractions, f_V and f_M , of gas with various densities:

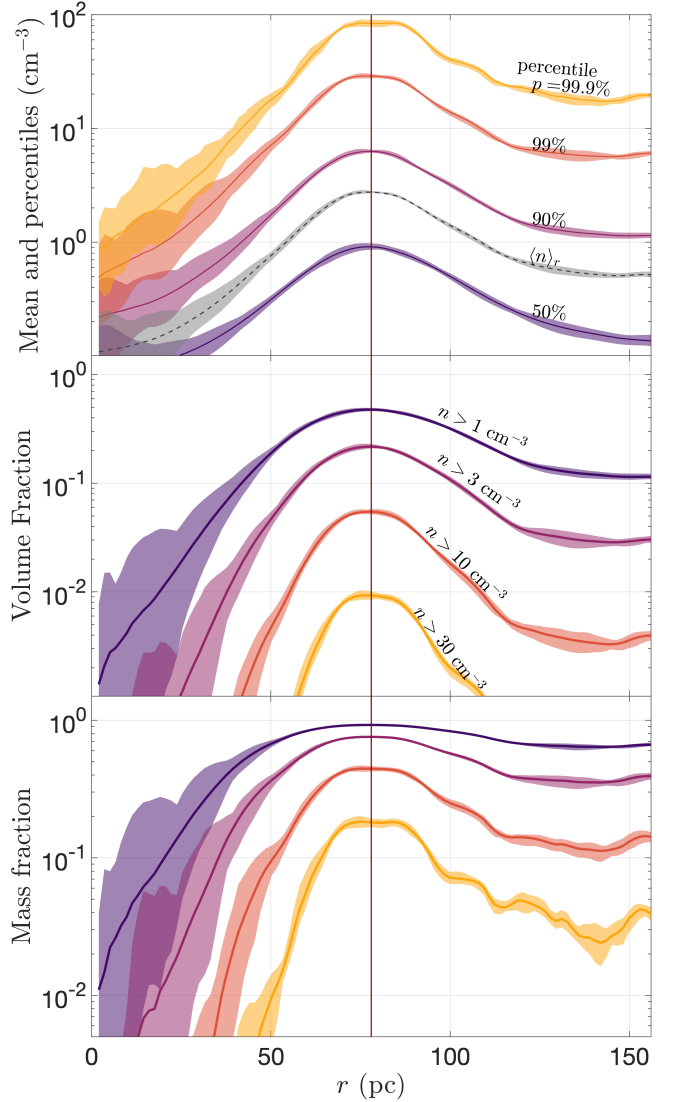


FIG. 3.— The Per-Tau Shell Radial Profile. The abscissa is the radial distance from the shell’s center and the vertical line is its modeled radius (Table 1). **Top:** The mean density (dashed), and different density percentiles (solid). **Middle and Bottom:** Volume and mass filling fractions for gas with different densities. In all panels, all quantities are computed within thin concentric spherical shells (see Appendix A). The shaded regions are the minimum-to-maximum variation across different dust-map samples, showing the uncertainty associated with the 3D data (see Appendix A).

$n > 1, 3, 10, 30 \text{ cm}^{-3}$ (Appendix A). Since f_V is calculated within thin shells, it also approximately equals the area covering fraction of gas with density $> n$ at each radius. All f_V curves fall rapidly at small radii, within the shell void ($r \ll R_s$), as well as at higher radii ($r \gg R_s$), albeit more gradually. Even at shell’s peak, the denser gas occupies only a small fraction of the volume (and area). However, in terms of mass fraction, the denser gas is significant. For example, at the shell radius $n > 30 \text{ cm}^{-3}$ gas accounts for $\approx 20\%$ of the mass, and \approx half the gas has density $> 10 \text{ cm}^{-3}$. This is in strong contrast with the central region (the void), which consists of mainly diffuse $n \ll 1 \text{ cm}^{-3}$ gas. The flat maximum (width $\approx 20 \text{ pc}$) results from the Per-Tau Shell having a complex ovaloid shape rather than a perfect sphere (e.g., see Fig. 2, lower-right panel).

In all panels, the shaded strips about each curve show the maximum and minimum values as obtained from each of the

twelve samples presented in L20, providing a measure of the uncertainty associated with L20’s 3D dust map (Appendix A). At small radii the spread is large as the statistics include only a small number of voxels, and thus the effect of fluctuations within the samples becomes significant. However, as r increases these fluctuations become insignificant.

3.4. 2D observations

3.4.1. Dust and CO: Comparing 3D to 2D

Fig. 4a shows the Planck $E(B - V)$ dust map tracing the integrated dust column density along the LOS, along with ^{12}CO . The 2D projections of the Per Tau Shell and the Tau Ring models are shown (Table 1). While the Tau Ring is partially traced by CO, the Per-Tau Shell is not identified in the 2D dust map or CO. This is because these 2D maps probe the integrated column along the LOS, and thus are much more sensitive to dense (high column density) structures. The limb brightening that may have revealed the shell contour is not effective because the large-scale structure of the shell consists of mainly diffuse gas ($n \sim 5 \text{ cm}^{-3}$) and the associated column density is low, comparable to that of the ambient ISM.

Planck’s $E(B - V)$ dust map is also shown in Fig. 1. Comparing the right and left panels we see that the 3D projected structures trace well known features seen in Planck (see also Fig. 6 and Zucker et al. 2021). However, the 3D dust includes distance information, providing additional insights:

1. *Taurus and Perseus*: The Taurus and Perseus molecular clouds are located at distances of $d \approx 150$ and 300 pc, from the sun (in agreement with Zucker et al. 2020), and are placed at the front and at the back sides of the Per-Tau Shell.
2. *Tau Ring*: In a sky projection the Tau Ring is seen almost edge-on. The near side of the Tau Ring connects with the main body of Taurus at $d \approx 150$ pc, whereas the farthest part extends to $d \approx 220$ pc.
3. *The Fictitious Connection*: A filament seems to connect Taurus to Perseus. This connection is only a coincidental projection effect, where in actuality the filament is located at the distance of Taurus, and does not physically connect to Perseus. This coincidence is even more striking given that the connection not only occurs in 2D position, but also in velocity space (i.e., see ^{12}CO , $v = 6.5$ km/s channel map in Fig. 4). This emphasizes how misleading it is to infer 3D structures from PPV data alone.

3.4.2. Tracing SN feedback: HI, H α , ^{26}Al , and X-rays

Fig. 4b shows HI4PI’s HI channel map ($v = -1.2$ km/s) of the Per-Tau region. The prominent HI void (as indicated) was studied previously by Sancisi (1974). From the semi-circular arcs seen in the HI channel maps and the expansion signatures seen in $p - v$ diagrams, they concluded that the HI forms an expanding shell of radius $R \approx 20$ pc, potentially powered by previous SN which has exploded $\approx 1 - 4$ Myr ago (see also Lim et al. 2013; Shimajiri et al. 2019).

Within the HI cavity, there is a peak in H α emission (Fig. 4c). The bright H α spot at $l \approx 162^\circ$, $b = -12^\circ$ is unrelated to the Per-Tau shell as it originates from the California nebula at a larger distance. Ignoring the unfortunate California Nebula projection, Fig. 4 shows that H α essentially fills

the cavity evident in HI, consistent with the hypothesis of recent SN activity in the region.

Fig. 4d shows an ^{26}Al map. ^{26}Al is injected into the ISM mainly by massive stars via core collapse SN and in Wolf-Rayet (WR) winds (Prantzos & Diehl 1996; Diehl et al. 2004). We identify a blob of enhanced ^{26}Al emission near the center of the Per-Tau Shell ($l \approx 168^\circ$, $b \approx -25^\circ$). Assuming the blob is located at the distance of the shell’s center ($d = 225$ pc), and using a distance-flux scaling based on observations of the Orion-Eridanus region (Diehl 2002), we obtain an ^{26}Al mass of $\approx 6 \times 10^{-5} M_\odot$, consistent with production by WR stars or SN (Limongi & Chieffi 2006). As there are no living WR stars within the shell, and given that ^{26}Al ’s half-lifetime is 0.7 Myrs, the observed emission suggests recent SN activity over the last few Myrs.

Fig. 4(e-f) show ROSAT’s 1/4 and 3/4 keV diffuse X-ray emission. We find an enhancement of X-ray emission near Per-Tau shell’s projected center (red circle). We have also identified an X-ray enhancement at a similar position in eROSITA’s all-sky map (see Appendix D). This diffuse X-ray emission (radius $\approx 7^\circ$) points towards the existence of hot gas potentially produced by past SN(e) on a timescale of a Myr (or less; Krause et al. 2014). Given the proximity to the HI void, the X-ray blob and the HI void may have resulted from the same SN event.

4. DISCUSSION

We have shown that the ISM in the Perseus-Taurus region has the structure of a large nearly spherical shell of radius $R_s \approx 78$ pc, encompassing the molecular clouds Taurus and Perseus, which are located at the near and far sides of the shell, at $d \approx 150$ pc, and ≈ 300 pc. The Taurus cloud also extends to larger distances, forming an extended ellipsoidal ring with semi-major and semi-minor axis $a \approx 39$ pc, $b \approx 26$ pc (Table 1 and Appendix B).

Recently, Doi et al. (2021) also mentioned the presence of a large dust cavity, as seen in the previous, lower resolution Leike & EnBlin (2019) map. However, as their focus is on the magnetic fields in the region, they did not study the 3D density structure in detail as is done here, nor did they explore potential mechanisms for forming this structure. As they show, the bimodal distribution of polarization angles supports the idea that Perseus and Taurus are well separated along the LOS.

In the remainder of this section we discuss a physical scenario for the formation of the Per-Tau Shell via gas compression and cooling in the swept-up shell of an expanding SB, and the implications for star formation (positive) feedback. We also estimate the shell’s age, and momentum and energy sources.

4.1. A Formation Scenario for the Per-Tau Shell

The shell’s near-spherical geometry, prominent dust free cavity, and large extent suggest a scenario in which the Per-Tau Shell has formed via multiple SN episodes, driving an expanding SB, sweeping up ISM into an extended shell. The HI, ^{26}Al and X-ray observations discussed in §3.4.2 further support this scenario. As discussed in §1, expanding shells may promote the formation of cold and molecular gas, and star formation. Indeed, the Per-Tau shell includes the Perseus and Taurus clouds, which are dense, molecule-rich gas clouds, which are actively forming stars.

However, there are no signatures of shell expansion: the Perseus and Taurus clouds are located on two opposite sides

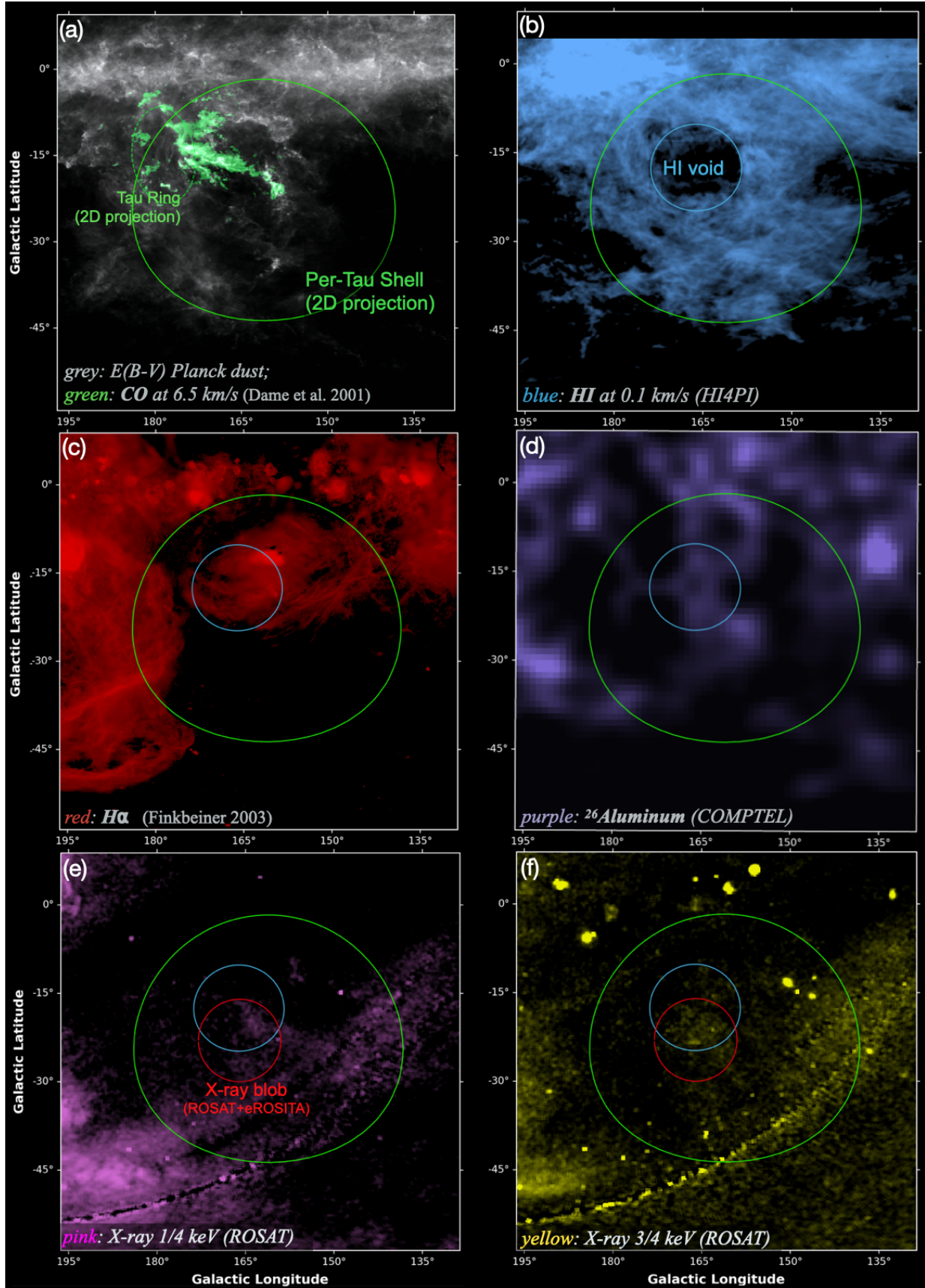


FIG. 4.— The Per-Tau region in different tracers: (a): Planck's $E(B-V)$ dust (Abergel et al. 2014) and Dame et al. (2001)'s ^{12}CO . 2D projections of the Per-Tau Shell and the Tau Ring models are shown. (b): HI4PI's HI map (Bekhti et al. 2016). (c): Finkbeiner (2003)'s $H\alpha$ map. (d): COMPTEL's ^{26}Al map (1.8 MeV γ -ray; Diehl et al. 1995). (e-f): ROSAT's X-ray 1/4, and 3/4 keV (Snowden et al. 1997) (see also Fig. 7 for eROSITA's observations). The HI void and the X-ray emission blob (see also Appendix D) are indicated. The HI void, ^{26}Al , $H\alpha$ and X-ray observations suggest recent SN activity in the region (see §3.4.2).

of the shell (along the LOS), but their CO radial velocities are similar to within a few km/s. The lack of expansion is also suggested by the 3D space motions of young stars in the two clouds (Ortiz-León et al. 2018; Galli et al. 2019). Thus, in this scenario, the Per-Tau Shell must be an old remnant, which has already decelerated below the turbulent velocity dispersion of the ISM, $v_{\text{turb}} \approx 7$ km/s, and is now dominated by gas dynamics of the surrounding ISM. Indeed, the ISM is expected to be abundant in such old bubbles due to the large volume they occupy and the long time spent in the evolved stage (McKee & Ostriker 1977; Cox 2005). The evolved stage is also the time at which there is higher probability for observing dense molecular gas, and star-formation in the shell, as sufficient time has passed to allow cooling to low temperatures, molecule-formation, and gravitational collapse.

4.2. Timescales

We can obtain an estimate for the Per-Tau Shell's age from its observed radius and lack of radial expansion. Theoretical models of an expanding SN remnant into a uniform medium find $R \propto t^\eta$ with $\eta = 0.25 - 0.3$ at late stages (at the snow-plow phase; Cioffi et al. 1988; Kim & Ostriker 2015; Haid et al. 2016). For a more realistic scenario of a SB powered by multiple SN $\eta \approx 0.5$ (Kim et al. 2017; El-Badry et al. 2019, see, e.g., Fig. 6 in the latter paper). The expansion velocity evolves as $v_{\text{exp}} = \eta(R/t)$, and the shell age is

$$t = \eta \frac{R}{v_{\text{exp}}} = 5.5 \left(\frac{\eta}{0.5} \right) \left(\frac{R}{78 \text{ pc}} \right) \left(\frac{v_{\text{exp}}}{7 \text{ km/s}} \right)^{-1} \text{ Myr}. \quad (2)$$

Here we normalized R to the observed shell's radius, and the expansion velocity to $v_{\text{turb}} = 7$ km/s, a typical value for the turbulent velocity dispersion (also comparable to the ambient WNM sound speed). Setting $v_{\text{exp}} = v_{\text{turb}}$ in Eq. (2) we get a lower limit for the shell's age, $t_{\text{min}} \approx 6$ Myr. This is a lower limit because, in practice the shell does not expand today, and the point at which it decelerated to $v = v_{\text{turb}}$ has occurred in the past, an unknown amount of time ago.

On the other hand, the shell cannot be too old, as otherwise the surrounding ISM would have filled the void inside the shell. The characteristic timescale for this process is the turbulent turnover time,

$$t = \phi \frac{R}{v_{\text{turb}}} = 21.8 \left(\frac{\phi}{2} \right) \left(\frac{R}{78 \text{ pc}} \right) \left(\frac{v_{\text{turb}}}{7 \text{ km/s}} \right)^{-1} \text{ Myr}, \quad (3)$$

where ϕ is a factor of order unity that accounts for the uncertainty in this simplistic description. For a conservative upper limit we adopt $\phi = 2$, giving $t_{\text{max}} \approx 22$ Myrs. The Per-Tau Shell age is thus bracketed $t_{\text{age}} \approx (6 - 22)$ Myrs.

Our derived age is long compared to the stellar ages of Perseus and Taurus (Bally et al. 2008; Luhman 2018), consistent with the scenario where the clouds and subsequent stars have formed in the shell. t_{age} is also long compared to the timescales of feedback traced by the HI, ^{26}Al and X-rays observations (see §3.4.2). This suggests that not one, but several SNe have probably contributed to the inflation of the Per-Tau Shell. In this picture, t_{age} is the time when the first SN(e) went off, whereas HI, ^{26}Al and X-rays trace more recent feedback activity, within the last ~ 1 Myr, in line with SN clustering (Wit et al. 2004; Fielding et al. 2018).

4.3. Momentum and Energy Sources

Simulations of clustered SNe exploding find that the momentum imparted into the ISM, per SN, is $\hat{p} = (3 - 6) \times 10^5 M_\odot \text{ km/s}$ for SN frequency of 1/Myr (El-Badry et al. 2019). For the Per-Tau Shell, we calculate the swept-up mass, M , by integrating the density (as given by the 3D density cube; §2) inside a sphere of radius R , and multiplying it by a mean particle mass $\langle m \rangle = 1.4m_{\text{H}}$. To have a handle on the uncertainty we perform the calculation for two different radii: $R = 94$ pc and 117 pc, corresponding to 1.2 and 1.5 R_s where $R_s = 78$ pc is the density-peak radius. These values are motivated by the gradual decrease of the radial profiles in Fig. 3. We obtain $M = (1.7 - 3.2) \times 10^5 M_\odot$, respectively. The associated momentum is

$$p = Mv_{\text{exp}} = (1.2 - 2.3) \times 10^6 \left(\frac{v_{\text{exp}}}{7 \text{ km/s}} \right) M_\odot \text{ km/s}. \quad (4)$$

Dividing by \hat{p} , we get that the corresponding number of SNe is

$$N_{\text{SN}} = \frac{p}{\hat{p}} = (2 - 8) \left(\frac{v_{\text{exp}}}{7 \text{ km/s}} \right). \quad (5)$$

The (2-8) range corresponds to the maximum mutual uncertainty range for $M(r)$ and \hat{p} . In practice, since the expansion velocity has already decreased below the 7 km/s level, Eqs. (4-5) are upper limits on p and N_{SN} .

The total mass of the star cluster required to produce these SNe can be estimated by assuming an IMF and a distribution of massive star lifetimes. For the Chabrier (2003) IMF, a star cluster of mass M_* produces in total $\sim 0.01(M_*/M_\odot)$ SNe. Assuming the stellar lifetime-mass relation for solar metallicity from Raiteri et al. (1996), we estimate that $\sim 15\% - 65\%$ of these SNe explode by 6 - 22 Myr, the age of the shell. For $N_{\text{SN}} \sim 5$ (the average from Eq. 5), these numbers correspond to a total star cluster mass of $M_* \sim 800 - 3300 M_\odot$.

Note however, that these estimations for N_{SN} and M_* may be considered upper limits, since they are based on simulations where \hat{p} is likely underestimated. First, these simulations lack stellar winds and radiation pressure which can inject momentum into the ISM at a rate comparable with SNe (e.g., Agertz et al. 2013). Second, they do not include the non-thermal pressure exerted by cosmic rays, which can boost the momentum injected per SN by a factor of a few (Diesing & Caprioli 2018, see their Fig. 3). Finally, the momentum per-SN may be underestimated due to excessive numerical mixing of the superbubble material with the surrounding ISM (e.g., Gentry et al. 2019).

Where are the remnants of the stellar cluster where the powering SN went off? Two recent studies have identified young populations inside the Per-Tau shell, with *Gaia*. Pavlidou et al. (2021) reported the discovery of five new stellar groups in the vicinity of the Perseus cloud ages between 1 - 5 Myr. Kerr et al. (2021) characterized all young stars in the local neighborhood. Their results suggest that there are at least two young (age < 20 Myr) populations located inside the Per-Tau shell. Pre-*Gaia*, Mooley et al. (2013) identified several B- and A-stars towards the Taurus clouds, consistent with the existence of a young population inside the Per-Tau, likely the more massive counterparts of the recently discovered *Gaia* populations. A dedicated study of young stars inside Per-Tau is currently missing, and the insights brought by the finding in this paper make such a study a priority for the near future.

Given the large uncertainty in the estimate of N_{SN} , an alternative scenario that does not require a star cluster within

Per-Tau is that the Per-Tau Shell has been produced by only a single SN explosion. Such a SN can result from an O or B star dynamically ejected from a nearby star-forming region. A more exotic possibility is that the Per-Tau bubble is a relic of a previous ultraluminous X-ray source (ULX). ULXs are often surrounded by hot ionized gas bubbles, thought to be powered by strong winds and radiation pressure (e.g., Pakull & Mirioni 2001; Kaaret et al. 2017; Sathyaprakash et al. 2019; Fabrika et al. 2021). However, since ULXs are extraordinarily rare, this possibility is rather unlikely.

5. CONCLUSIONS

In this paper we explored the 3D structure of the Perseus and Taurus region. Our conclusions are

1. The Perseus and Taurus molecular clouds are not independent, but are part of a larger structure, the “Per-Tau Shell”, an extended shell of radius 78 pc, centered in-between the two clouds at a distance $d = 218$ pc.
2. The 3D observations further reveal a prominent ring

structure connecting to Taurus, the “Tau Ring”, with semi-major and semi-minor axes, $a = 39$ pc, $b = 26$ pc, oriented nearly edge-on and is partially traced by CO.

3. The densest structures in the 3D map have good correspondence with known features in the 2D dust and CO, but diffuse structures (such as the Per-Tau Shell) are not identified in 2D as the integration along the LOS results in significant blending with the ambient ISM.
4. $H\alpha$, Soft X-ray, and ^{26}Al enhancements, as well as a void of HI, are seen in different locations within the Per-Tau Shell, suggesting recent SN activity.

Based on these observations we propose a formation scenario for the Per-Tau Shell by multiple SNe and other forms of stellar feedback activity occurring within the last $\approx 6 - 22$ Myrs. This feedback inflated an expanding shell of compressed cooled gas, potentially leading to the formation of the Taurus and Perseus molecular clouds. This points to the positive aspect of stellar/SN feedback, promoting cloud formation and star formation in expanding superbubbles.

APPENDIX

A. METHODS

Radial Mean Density: To characterize the structure of the Per-Tau shell we calculate the radial-mean density profile, defined as:

$$\langle n \rangle_r(r) \equiv \frac{\sum_{r' \in (r-\delta r/2, r+\delta r/2)} n(r')}{\sum_{r' \in (r-\delta r/2, r+\delta r/2)} 1}. \quad (\text{A1})$$

Here r is the radial distance from Per-Tau shell’s center. At each radius, the density is averaged over a thin radial shell of radius r and width δr . We choose $\delta r = 10$ pc, large compared to the data resolution (1 pc). This (1) reduces inaccuracies resulting from the misalignment of the Cartesian grid of the data with the spherical geometry of the averaging window, and (2) allows having a sufficiently large number of voxels for calculating statistics. We also experimented with other values for $\delta r = 5 - 20$, and verified that our results are insensitive to the exact value of δr . We compute $\langle n \rangle_r(r)$ as a function of r , for r ranging from 0 (shell’s center) to 140 pc.

Radial Percentiles and Volume and Mass Fractions: While $\langle n \rangle_r(r)$ is useful for exploring the general trend with radius, it gives only the mean density as a function of radius and does not include information on the density dispersion within each radius. To characterize the shell profile in more detail, we calculate density percentiles, and the volume and mass fractions. The density percentile $n_p(r)$ is computed as the density below which gas occupies the volume fraction p in a radial shell with radius r . For example, $n_{p=0.95}(r) = 10 \text{ cm}^{-3}$ means that at radius r , gas with $n < 10 \text{ cm}^{-3}$ fills 95% of the volume, whereas dense $n \geq 10 \text{ cm}^{-3}$ gas is rare and occupies only the remaining 5% of volume. In a similar manner, at any given radius r , the volume and mass fractions, $f_V(r; n')$ and $f_M(r; n')$, respectively, are the fractions of the volume and mass at that radius, occupied with gas denser than n' . Similarly to the calculation of $\langle n \rangle_r(r)$, we calculate n_p , f_V and f_M , within thin radial shells of radii r (ranging from 0 to 140 pc), and width $\delta r = 10$ pc.

Uncertainties in the 3D Dust Map: L20 presented twelve posterior samples for the dust opacity density, representing possible realizations of the underlying 3D dust distribution. While the samples are statistically similar, they differ in the density they predict on a voxel-by-voxel basis. For the radial profiles discussed above. we repeat our calculation for each of the twelve samples provided by L20. In §3, we present the mean profiles, averaged over the sample results, as well as the minimum-maximum ranges for the twelve samples. The dispersion over the samples provides a handle on the uncertainty associated with the reconstruction method adopted by L20. Otherwise, where statistical calculations are not involved, we utilize the mean dust map in which the density is averaged over the samples.

B. THE TAU RING AND ADDITIONAL 3D VISUALIZATIONS

In Fig. 5 we show additional 3D visualizations of the dust in the Perseus-Taurus region as seen from different observational orientations. Our model of the Per-Tau shell is also shown (Table 1). In the bottom-left panel we show a 2D plane that cuts through the Tau Ring. The plane is spanned by the two basis vectors:

$$\hat{e}_1 = (0.923, 0.353, -0.154), \quad \hat{e}_2 = (0.005, 0.302, 0.841), \quad (\text{B1})$$

in Heliocentric Cartesian Galactic coordinates. The origin of the basis vectors, and the Tau ring, is located at

$$\vec{r}_0 = (-174, 1, -44) \text{ pc}. \quad (\text{B2})$$

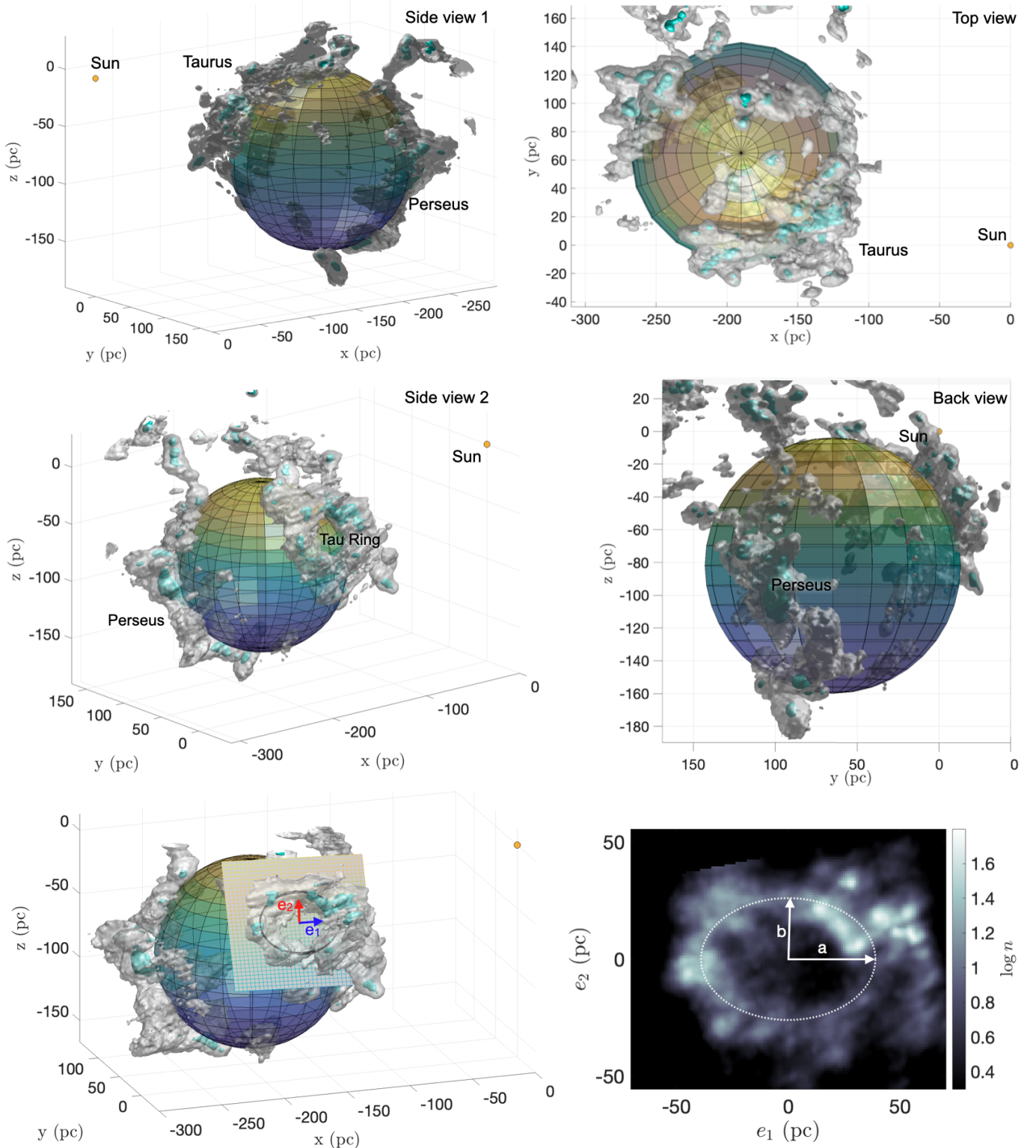


FIG. 5.— 3D view of the Perseus Taurus region in 3D dust. **Top Panels:** Shown are iso-surfaces at $n = 5 \text{ cm}^{-3}$ (grey) and $n = 25 \text{ cm}^{-3}$ (cyan) levels. The colored sphere is the sphere model of the Per-Tau shell (Table 1). **Bottom Panels:** The Tau Ring. A plane cutting through the Tau Ring (left), the basis vectors spanning the plane (**B1**) are also shown. On the Right we show a density slice through the $\hat{e}_1 - \hat{e}_2$ plane. The modeled ellipse with semi-major axis $a = 39 \text{ pc}$ and semi-minor axis $b = 26 \text{ pc}$ is shown.

The $\hat{e}_1 - \hat{e}_2$ basis vectors are shown as the blue and red vectors in the lower-left panel of Fig. 5. Any point on the $\hat{e}_1 - \hat{e}_2$ plane is described by $\vec{r} = \hat{e}_1 s + \hat{e}_2 t + \vec{r}_0$ where s, t are some real numbers. In the bottom-right panel we show a density cut through the $\hat{e}_1 - \hat{e}_2$ plane. We model the Tau Ring as an ellipse with semi-major axis $a = 39 \text{ pc}$ and semi-minor axis $b = 26 \text{ pc}$. The basis vectors $\hat{e}_1 - \hat{e}_2$ were constructed to be parallel with the ellipse's semi-major and semi-minor axis, respectively. Thus, Tau Ring's

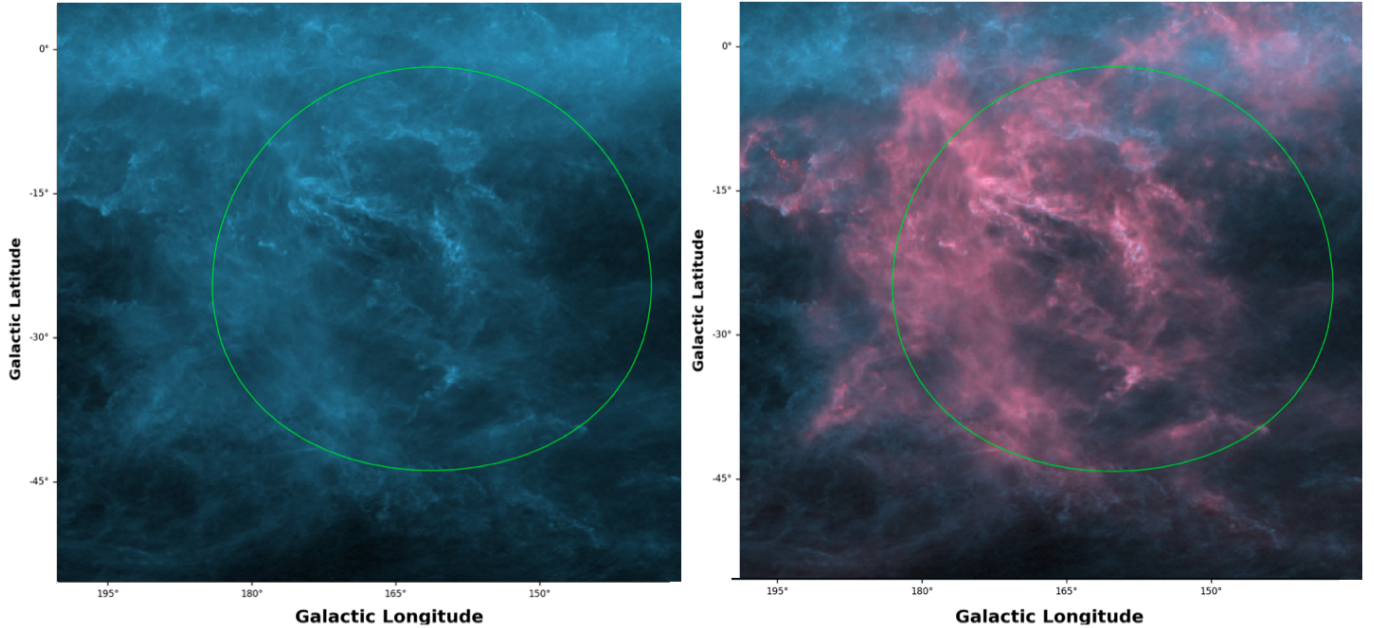


FIG. 6.— Comparing 3D dust to 2D dust. Left: The Planck $E(B-V)$ dust map (in blue) tracing the total dust column density integrated along the LOS. Right: The Planck $E(B-V)$ dust map overlaid with the projection of the 3D dust map (in red) on the plane of the sky. The two maps are in excellent agreement. The 3D dust includes all dust within the L20 3D map limits (e.g., the California Nebula which is located at a larger distance is excluded and does not show in red).

3D orientation is fully defined by \hat{e}_1, \hat{e}_2 (Eq. B1).

C. FURTHER 2D-3D DUST COMPARISONS

In Fig. 6 we show a comparison of 2D and 3D dust. In the left panel we show the Planck $E(B-V)$ dust map in blue. In the right panel we overlay Planck’s map with a projected 3D dust map (in red). The two are in excellent agreement. The advantage of 3D dust is that it includes information on the distance, so we can exclude foreground and background material in the 3D projected maps. For example, the map shown in Fig. 6 does not show the background California Nebula.

D. E-ROSITA X-RAY OBSERVATIONS

In Fig. 7 we show eROSITA’s soft X-rays all-sky map (originally published online⁸), and a zoom-in onto the region of the Per-Tau shell. The green oval is the projection of the Per-Tau shell (the distorted shape is due to map projection effects). We identify a blob of enhanced X-ray emission within the Per-Tau Shell in both ROSAT and eROSITA. This is shown as the red oval in Fig. 7, as well as in panels (e,f) in Fig 4.

The authors thank Roland Diehl for making the COMPTEL γ -ray map accessible to us, Peter Williams for helping with coordinate projections of the ROSAT data, and the anonymous referee for useful comments. SB. thanks Drummond Fielding, Shu-ichiro Inutsuka, Munan Gong, and Enrique Vazquez-Semadeni for insightful discussions. The authors are thankful to Eugene Belyaev and the *Delightex* team for developing the augmented reality (AR) figure. The authors also thank Ian Masson for developing functionality to enable export of the data into AR-compatible formats. SB acknowledges the Institute for Theory and Computations (ITC) at the Harvard-Smithsonian Center for Astrophysics for financial support. The visualization, exploration, and interpretation of data presented in this work was made possible using the *glue* visualization software, supported under NSF grant numbers OAC-1739657 and CDS&E:AAG-1908419. The interactive component of Figure 2 was created using the visualization software (plot.ly).

REFERENCES

- Abergel, A., Ade, P. A., Aghanim, N., Alves, M. I., Aniano, G., Armitage-Caplan, C., Arnaud, M., Ashdown, M., & et al. . 2014, *A&A*, 571, 1
- Agertz, O., Kravtsov, A. V., Leitner, S. N., & Gnedin, N. Y. 2013, *ApJ*, 770
- Audit, E. & Hennebelle, P. 2005, *A&A*, 433, 1
- Bally, J., Walawender, J., Johnstone, D., Kirk, H., & Goodman, A. 2008, *Handb. Star Form. Reg.*, 4
- Bekhti, B., Flöer, L., Keller, R., Kerp, J., Lenz, D., Winkel, B., Bailin, J., Calabretta, M. R., Dedes, L., Ford, H. A., Gibson, B. K., Haud, U., Janowiecki, S., W Kalberla, P. M., Lockman, F. J., McClure-Griffiths, N. M., Murphy, T., Nakanishi, H., Pisano, D. J., & Staveley-Smith, L. 2016, *A&A*, 594, 116
- Bialy, S. & Burkhart, B. 2020, *ApJ*, 894, L2
- Bialy, S. & Sternberg, A. 2019, *ApJ*, 881, 160
- Brown, A. G. A., Vallenari, A., Prusti, T., J. D. B. J. H., & et al. Babusiaux, C. 2018, *A&A*, 616, A1
- Chabrier, G. 2003, *Publ. Astron. Soc. Pacific*, 115, 763
- Chen, B. Q., Huang, Y., Yuan, H. B., Wang, C., Fan, D. W., Xiang, M. S., Zhang, H. W., Tian, Z. J., & Liu, X. W. 2019, *MNRAS*, 483, 4277

⁸ <https://www.mpe.mpg.de/7461761/news20200619>

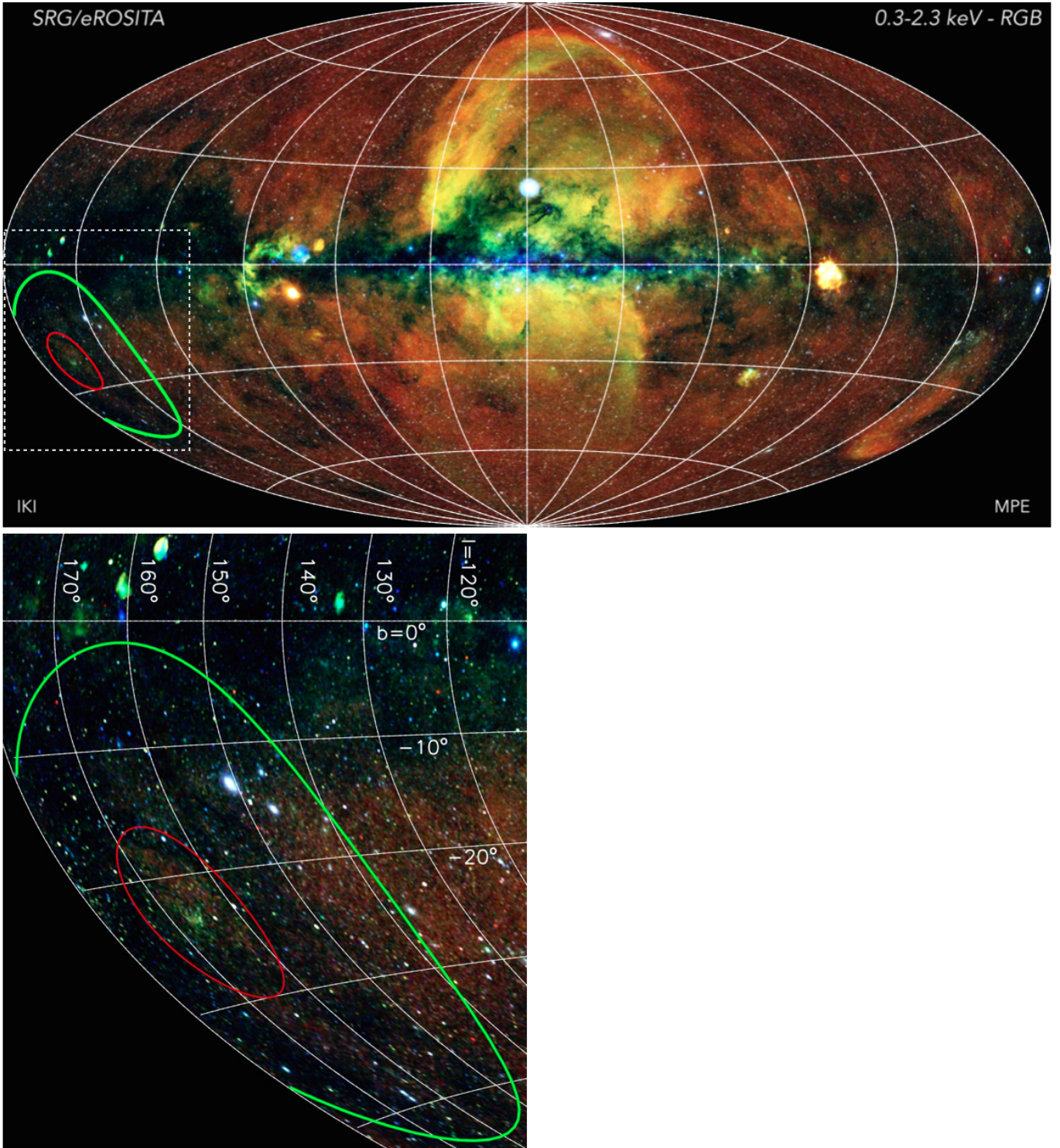


FIG. 7.— eROSITA's soft X-ray image of the Per-Tau region (originally published online⁸). The RGB colors correspond to X-ray energies, from 0.2 keV (red) to 2.3 keV (blue). The green oval is the projected Per-Tau shell outline (the distorted shape is a result of the Aitoff map projection of eROSITA's all sky map). The red oval within the Per-Tau shell, highlights a region of enhanced X-ray emission, which is also seen in the ROSAT X-ray data (see Fig. 4 panels e-f).

- Cioffi, D. F., Mckee, C. F., & Bertschinger, E. 1988, *ApJ*, 334, 252
- Cox, D. P. 2005, *ARA&A*, 43, 337
- Dame, T. M., Hartmann, D., & Thaddeus, P. 2001, *ApJ*, 547, 792
- Dawson, J. R. 2013, *Publ. Astron. Soc. Aust.*, 30, e025
- Dawson, J. R., Kawamura, A., Mizuno, N., Onishi, T., Mizuno, A., & Fukui, Y. 2011, *ApJ*, 728, 127
- Dawson, J. R., Ntormousi, E., Fukui, Y., Hayakawa, T., & Fierlinger, K. 2015, *ApJ*, 799, 64
- Diehl, R. 2002, *New Astron. Rev.*, 46, 547
- Diehl, R., Cerviño, M., Hartmann, D. H., & Kretschmer, K. 2004, *New Astron. Rev.*, 48, 81
- Diehl, R., Dupraz, C., Bennett, K., & Bloemen, H. 1995, *A&A*, 298, 445
- Diesing, R. & Caprioli, D. 2018, *Phys. Rev. Lett.*, 121, 91101
- Doi, Y., Hasegawa, T., Bastien, P., Tahani, M., Arzoumanian, D., Coudé, S., Matsumura, M., Sadavoy, S., Hull, C. L. H., Shimajiri, Y., Furuya, R. S., Johnstone, D., Plume, R., Inutsuka, S.-i., Kwon, J., & Tamura, M. 2021, *arXiv:2104.11932*
- Draine, B. T. 2011, *Physics of the interstellar and intergalactic medium*
- El-Badry, K., Ostriker, E. C., Kim, C.-G., Quataert, E., & Weisz, D. R. 2019, *MNRAS*, 490, 1961
- Elmegreen, B. G. 2011, *EAS Publ. Ser.*, 51, 45
- Fabrika, S. N., Atapin, K. E., Vinokurov, A. S., & Sholkhova, O. N. 2021, *Astrophys. Bull.*, 76, 6
- Federrath, C., Klessen, R. S., & Schmidt, W. 2008, *ApJ*, 688, L79
- Field, G. B., Goldsmith, D. W., & Habing, H. J. 1969, *ApJ*, 155, L149
- Fielding, D., Quataert, E., & Martizzi, D. 2018, *MNRAS*, 481, 3325
- Finkbeiner, D. P. 2003, *ApJS*, 146, 407
- Galli, P. A., Loinard, L., Bouy, H., Sarro, L. M., Ortiz-León, G. N., Dzib, S. A., Olivares, J., Heyer, M., Hernandez, J., Román-Zúñiga, C., Kounkel, M., & Covey, K. 2019, *arXiv*, 137, 1
- Gentry, E. S., Krumholz, M. R., Madau, P., & Lupi, A. 2019, *MNRAS*, 483, 3647
- Green, G. M., Schlafly, E., Zucker, C., Speagle, J. S., & Finkbeiner, D. 2019, *arXiv*, 93
- Haid, S., Walch, S., Naab, T., Seifried, D., Mackey, J., & Gatto, A. 2016, *MNRAS*, 460, 2962
- Hartmann, L., Ballesteros-Paredes, J., & Bergin, E. A. 2002, *ApJ*, 562, 852
- Heitsch, F., Slyz, A. D., Devriendt, J. E. G., Hartmann, L. W., & Burkert, A. 2006, *ApJ*, 648, 1052
- Hennebelle, P. & Inutsuka, S.-I. 2019, *Front. Astron. Sp. Sci.*, 6
- Hennebelle, P. & Pérault, M. 1999, *A&A*, 351, 309
- Hosokawa, T. & Inutsuka, S.-i. 2006, *ApJ*, 648, L131
- Inoue, T. & Inutsuka, S. 2008, *ApJ*, 687, 303
- Inoue, T. & Inutsuka, S. I. 2009, *ApJ*, 704, 161
- Inutsuka, S. I., Inoue, T., Iwasaki, K., & Hosokawa, T. 2015, *A&A*, 580, A49
- Kaaret, P., Feng, H., & Roberts, T. P. 2017, *ARA&A*, 55, 303
- Kerr, R., Rizzuto, A. C., Kraus, A. L., & Offner, S. S. R. 2021, *arXiv:2105.09338*
- Kim, C. G. & Ostriker, E. C. 2015, *ApJ*, 802, 99
- Kim, C.-G., Ostriker, E. C., & Raileanu, R. 2017, *ApJ*, 834, 25
- Koyama, H. & Inutsuka, S. 2000, *ApJ*, 1, 980
- , 2002, *ApJ*, 564, L97
- Krause, M., Diehl, R., Böhringer, H., Freyberg, M., & Lubos, D. 2014, *A&A*, 566, A94
- Kritsuk, A. G., Ustyugov, S. D., & Norman, M. L. 2017, *New J. Phys.*, 19, 065003
- Lallement, R., Babusiaux, C., Vergely, J. L., Katz, D., Arenou, F., Valette, B., Hottier, C., & Capitanio, L. 2019, *A&A*, 625, 1
- Lee, H. T. & Chen, W. P. 2009, *ApJ*, 694, 1423
- Leike, R., Glatzle, M., & Enßlin, T. A. 2020, *A&A*, 138, 1
- Leike, R. H. & Enßlin, T. A. 2019, *A&A*, 631, 1
- Lim, T. H., Min, K. W., & Seon, K. I. 2013, *ApJ*, 765, 107
- Limongi, M. & Chieffi, A. 2006, *ApJ*, 647, 483
- Luhman, K. L. 2018, *ApJ*, 156, 271
- Mackey, A. D., Kopusov, S. E., Da Costa, G. S., Belokurov, V., Erkal, D., Fraternali, F., McClure-Griffiths, N. M., & Fraser, M. 2017, *MNRAS*, 472, 2975
- McKee, C. F. & Ostriker, J. P. 1977, *ApJ*, 218, 148
- Mooley, K., Hillenbrand, L., Rebull, L., Padgett, D., & Knapp, G. 2013, *The Astrophysical Journal*, 771, 110
- Ntormousi, E., Burkert, A., Fierlinger, K., & Heitsch, F. 2011, *ApJ*, 731
- Ortiz-León, G. N., Loinard, L., Dzib, S. A., Galli, P. A., Kounkel, M., Mioduszewski, A. J., Rodríguez, L. F., Torres, R. M., Hartmann, L., Boden, A. F., Evans, N. J., Briceño, C., & Tobin, J. J. 2018, *arXiv*, 865, 73
- Pakull, M. W. & Mirioni, L. 2001, in *Symp. 'New Visions X-ray Universe Xmm-newt. Chandra Era'*
- Palouš, J. 2014, *Astrophys. Sp. Sci. Proc.*, 36, 181
- Pavlidou, T., Scholz, A., & Teixeira, P. S. 2021, *MNRAS*, 503, 3232
- Prantzos, N. & Diehl, R. 1996, *Phys. Rep.*, 267, 1
- Raiteri, C. M., Villata, M., & Navarro, J. F. 1996, *A&A*, 315, 105
- Sancisi, R. 1974, in *Galact. Radio Astron. Proc. from IAU Symp. no. 60 held Maroochydyore Queensland, Aust. 3-7 Sept. 1973*. Ed. by Frank J. Kerr Simon Christ. Simonson. *Int. Astron. Union. Symp. no. 60*, Dordrecht-Holland; B
- Sathyaprakash, R., Roberts, T. P., Walton, D. J., Fuerst, F., Bachetti, M., Pinto, C., Alston, W. N., Earnshaw, H. P., Fabian, A. C., Middleton, M. J., & Soria, R. 2019, *MNRAS*, 488, L35
- Saury, E., Miville-Deschênes, M.-A., Hennebelle, P., Audit, E., & Schmidt, W. 2014, *A&A*, 567, A16
- Seifried, D., Schmidt, W., & Niemeyer, J. C. 2010, *A&A*, 526
- Shimajiri, Y., André, P., Palmeirim, P., Arzoumanian, D., Bracco, A., Könyves, V., Ntormousi, E., & Ladjelate, B. 2019, *A&A*, 623
- Snowden, S. L., Egger, R., Freyberg, M. J., McCammon, D., Plucinsky, P. P., Sanders, W. T., Schmitt, J. H. M. M., Trumper, J., & Voges, W. 1997, *ApJ*, 485, 125
- Su, Y., Chen, Y., Yang, J., Koo, B.-c., Zhou, X., Jeong, I.-g., & Zhang, C.-g. 2009, *Astrophys. Journalastrop*, 694, 376
- Ungerechts, H. & Thaddeus, P. 1987, *ApJS*, 63, 645
- Vázquez-Semadeni, E., Ryu, D., Passot, T., Gonza, R. F., & Gazol, A. 2006, *ApJ*, 1, 245
- Wit, W. J., Testi, L., Palla, F., Vanzì, L., & Zinnecker, H. 2004, *A&A*, 425, 937
- Wolfire, M. G., McKee, C. F., Hollenbach, D., & Tielens, A. G. G. M. 2003, *ApJ*, 587, 278
- Zucker, C., Goodman, A. A., Alves, J., Bialy, S., Koch, E. W., Speagle, J. S., Foley, M., Finkbeiner, D. P., Leike, R. H., & Enßlin, T. A. 2021, *ApJ*. *Submitt.*
- Zucker, C., Speagle, J. S., Schlafly, E. F., Green, G. M., Finkbeiner, D. P., Goodman, A., & Alves, J. 2020, *A&A*, 633, 1